Echo occurrence in the southern polar ionosphere for the SuperDARN Dome C East and Dome C North radars

Maria Federica Marcucci, Igino Coco, Stefano Massetti, Alessio Pignalberi,
Victoriya Forsythe, Michael Pezzopane, Alexander Koustov, Simona Longo,
David Biondi, Enrico Simeoli, et al.

Echo occurrence in the southern polar ionosphere for the SuperDARN Dome C East and Dome C North radars

Maria Marcucci, Igino Coco, Stefano Massetti, Alessio Pignalberi, Victoriya Forsythe, Michael Pezzopane, Alexander Koustov, Simona Longo, David Biondi, Enrico Simeoli, et al.

Echo occurrence in the southern polar ionosphere for the SuperDARN Dome C East and Dome C North radars

Maria Federica Marcucci [a, *], Igino Coco [b], Stefano Massetti [a], Alessio Pignalberi [b], Victoriya Forsythe [c], Michael Pezzopane [b], Alexander Koustov [d], Simona Longo [e], David Biondi [a], Enrico Simeoli [f], Giuseppe Consolini [a], Monica Laurenza [a], Aurélie Marchaudon [g], Andrea Satta [h], Alessandro Cirioni [e], Angelo De Simone [i], Angelo Olivieri [f], Alessandro Baù [j], Alberto Salvati [f]

[a] *INAF-IAPS, Roma, Italy*
[b] *INGV, Roma, Italy*
[c] *ASTRA, LLC, Louisville, CO, USA*
[d] *ISAS-Univ. of Saskatchewan, Saskatoon, Canada*
[e] *CNR-DTA, Roma, Italy*
[f] *CNR-ICT, Roma, Italy*
[g] *IRAP, CNRS, Toulouse University, CNES, Toulouse, France*
[h] *CNR-IAS, Oristano, Italy*
[i] *CNR-ISMN, Roma, Italy*
[j] *Department of Physics, University of Milano Bicocca, Milano, Italy*

ABSTRACT

In this paper, echo occurrence rates for the Dome C East (DCE) and the new Dome C North (DCN) radars are studied. We report the ionospheric and ground scatter echo occurrence rates for selected periods around equinoxes and solstices in the final part of the solar cycle XXIV. The occurrence maps built in Altitude Adjusted Corrected Geomagnetic latitude and Magnetic Local Time coordinates show peculiar patterns highly variable with season. The comparisons of the radar observations with the International Reference Ionosphere model electron density and with ray tracing simulations allow us to explain the major features of observed patterns in terms of electron density variations. The study shows the great potential of the DCE and DCN radar combination to the Super Dual Auroral Radar Network (SuperDARN) convection mapping in terms of monitoring key regions of the high-latitude ionosphere critical for understanding of the magnetospheric dynamics.

1. Introduction

The Dome C East (DCE) and Dome C North (DCN) High Frequency (HF) radars are part of the Super Dual Auroral Radar Network (SuperDARN). DCE has been in operation since late January 2013 while DCN saw the first light on January 17, 2019 and has been regularly producing data since January 28, 2019. The two radars are located nearby the Southern geomagnetic Pole, at the Concordia research station (Antarctica, 75° 5′ 59.91″ S, 123° 19′ 57.38″ E). DCE and DCN, similarly to other SuperDARN radars, transmit multi-pulse signals along 16 beam directions and receive ionospheric echoes (in 45-km range gates) from the electron density decameter irregularities present in the ionosphere within radars' Field of View (FoV). Analysis of the autocorrelation function of the multi-pulse signal sequences permits to infer the power,

Doppler velocity, and spectral width of the echoes received from various ranges and beams enabling the monitoring of the dynamics of the E and F region plasma. DCE and DCN radars transmit signals from the geomagnetic Pole towards the southern auroral latitudes, so that the DCE and DCN beams have comparable orientation with respect to the auroral oval permitting "homogeneous" observations of the physical processes occurring in the E and F regions of the ionosphere. In this study, we investigate the echo occurrence (EO) for DCE and DCN radars. The EO from the ionosphere is affected by a number of physical processes in geospace: the ones that influence the ionosphere state, e. g., the overall ionospheric vertical and horizontal density distribution affecting the radar wave propagation, and those responsible for the electron density irregularity generation. Radio waves transmitted by an over-the-horizon radar are received back if at least two main conditions

are satisfied: the ionospheric electron density in the area reached by the radar waves has quasi-periodic irregularities that are able to produce constructive interference of back-scattered radar waves (1) and, since such irregularities are found to be stretched along the magnetic field lines, the transmitted radar waves, after refraction in the ionosphere, are bent to a propagation path that is perpendicular to the magnetic field lines and thus orthogonal to the irregularity plane so that the back scatter can occur (2, the so called orthogonality condition). Back scatter echoes can also originate from the ground once the transmitted waves, after strong refraction in the ionosphere, reach the Earth's surface where the terrain roughness/sea waves could facilitate the reflection of the waves. The study of EO helps to understand a number of issues related to the HF signal propagation and mechanisms of irregularity formation and also to give a correct interpretation of the nature of received HF coherent echoes. In addition, knowledge of the distribution of EO in terms of magnetic latitude and Magnetic Local Time (MLT) for an individual radar helps in quantifying its potential contribution to the network in terms of the data addition in various regions of the polar, auroral, and mid-latitude ionosphere. For these reasons, the EO statistics for SuperDARN radars has been studied since the network formation started from the few primeval radars in the late 1980s. Although the measurement of the bulk plasma motion in the ionosphere has been the primary goal for which the network was originally conceived and a variety of phenomena have been investigated in subsequent years (Greenwald et al., 1995; Chisham et al., 2007; Nishitani et al., 2019), the identification of the factors influencing the EO and their interplay have not been fully achieved yet. Past studies clearly evidenced that SuperDARN EO rates strongly depend on the radar location, radar operating frequency, hour of the day, season, and phase of the solar cycle (e.g., Ruohoniemi and Greenwald, 1997; Milan et al., 1997; Danskin et al., 2002; Koustov et al., 2004; Prikryl et al., 2010; Hosokawa and Nishitani, 2010; Bristow et al., 2011; Ghezelbash et al., 2014a; 2014b; Lamarche and Makarevich, 2015). Recently, Koustov et al. (2019) presented a comprehensive study of the occurrence of F region echoes for the polar cap SuperDARN radars. These authors analysed the observations provided by three SuperDARN radars in the Northern polar cap, in the years 2008–2017 and by three SuperDARN radars in the Southern polar cap, in the years 2013–2017. Because of the long-time coverage of their data, they were able to assess the F region EO rates over solar, seasonal, and diurnal cycles. Their study included the DCE observations. Using the whole data set from the six radars, they found that the EO rates of the radars decreased by 5–10% per year over the descending phase of the last solar cycle and concluded that this is mainly caused by a decrease of the F region electron density. They also confirmed the previously reported result that the EO rates are highest in winter and equinoxes and lowest in summer. Regarding the relationship between the EO and the electron density, they found that the EO saturates for electron density above a threshold value that depends on season, local time, and average plasma flow velocity magnitude. Koustov et al. (2019) considered a selection of beams and gates for each of the polar cap radars. In the case of DCE, the ionospheric echoes occurrence was studied for beams 10–12 and gates 10–30.

Here we present a study of the DCE and DCN EO rates of the ionospheric scatter (IS) and ground scatter (GS) echoes considering the entire radars' FoVs and analysing the radars' IS and GS rates distribution as a function of magnetic latitude and MLT. In particular, we concentrate on how these distributions vary with season. We also investigate the EO dependence on radar frequency and geomagnetic activity.

2. Data set description

Alike most of the other SuperDARN radars, the DCE and DCN beams are separated by 3.3° so that the FoV of each of the two radars is about 50° wide in azimuth. Each range gate has a 45-km length. The first range gate starts at 180 km. The number of range gates is 75 or 100

and the back scatter signal can be received from a maximum distance from the radar of 3550 km or 4680 km, respectively. The radar usually scans the FoV in 1 or 2 min depending on the operation mode. In this study, we use the Chisham et al. (2008) model for the computation of the virtual height in order to obtain the geolocation of each beam-range cell. The observations are then represented in the Altitude Adjusted Corrected Geomagnetic coordinates system (Shepherd, 2014).

The DCE and DCN radars FoVs are shown in Fig. 1 for 11 February 2019, 12 UT. In Fig. 1, the 75 range case is presented. It can be noted, as previously pointed out, that DCE and DCN radar site location is such that the DCE and DCN FoVs extend evenly with respect to the AACGM coordinates, represented by solid grey lines in Fig. 1. We also note that the DCE and DCN beams are exposed differently when considering the solar illumination of the ionosphere. At each measurement, the cells move approximately 0.5° forward in longitude (rotating counterclockwise around the geomagnetic Pole, when looking down through the Earth from above the Northern Hemisphere). Therefore, a MLT-AACGMLAT (herein after MLT-MLAT, for the sake of brevity) map of the EO IS and GS rates distribution, extending in magnetic latitude from −89° to −59° (−50° MLAT when the radar operates with 75 ranges), can be computed for each beam in one day time.

To clearly infer the differences in the EO distribution in magnetic latitude and MLT due to the season, we consider observations over 14-day periods around equinoxes and solstices. First, the IS and GS echoes from each beam-range cell for each radar scan in the considered periods (echoes from the ranges of all 16 beams are considered) are binned into 1° MLAT x 5° MLON pixels. Then the IS and GS scattering rate (briefly the IS and GS rates) are computed as the ratios of the total number of counted IS and GS echoes to the total number of available soundings in each cell over the studied periods. To compute the significant back scatter, only echoes for which the back scatter power was greater than 3 dB were considered in the analysis.

In this study, the data analysis is based on the SuperDARN Radar Software Toolkit (RST; SuperDARN Data Analysis Working Group, 2017, 2018).
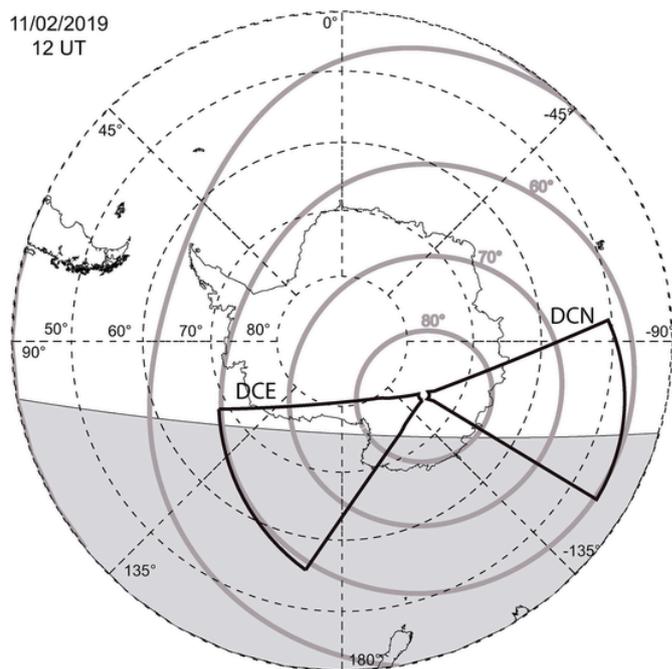

Fig. 1. The Dome C East (DCE) and Dome C North (DCN) radars Fields of View for February 11, 2019, 12 UT. The geographic coordinates system is represented by dashed lines. The AACGM magnetic latitudes are shown by solid grey lines. Solar noon is at the top, midnight at the bottom. The shaded region is the Earth's portion in darkness.

The DCE radar employed a unique mode of operation between January 2013 and December 2016 with the radar transmitting frequency being switched regularly between Frq1 ≃ 10 MHz and Frq2 ≃ 12 MHz at every next scan. We use DCE observations for this interval to perform a statistical study of the EO rates since they can be considered homogeneous in terms of mode of operation and used frequencies. Therefore, we compute the EO rates maps collecting the DCE echoes observed during a number of 14-days periods centered around equinoxes and solstices in the 2013–2016 interval. In total, sixteen periods should be present in the interval. Unfortunately, during 2015 a power outage occurred causing a failure of one element of the radar control system. This had severe consequences, as the radar operation was interrupted for almost 6 months, until it was possible to fix the failure during the following Antarctic summer campaign. Therefore, observations are only available for the Southern Hemisphere Spring equinox and Summer solstice in 2015 (from now on we will no more specify that equinoxes and solstice**s** are intended for the Southern Hemisphere). Moreover, during the second half of December 2013 the radar was not working for long intervals due to maintenance activities, so that observations are only available for the Autumn, Winter and Spring periods in 2013. Therefore, in order to keep approximately the same number of observation days for each season, we disregarded the 2015 Spring period and kept the 2015 Summer period. In this way, an even number of periods for each season is made available for the analysis. Namely, the dataset comprises three Autumn equinoxes (in 2013, 2014, 2016); three Winter solstices (in 2013, 2014, 2016), three Spring equinoxes (in 2013, 2014, 2016) and three Summer solstices (in 2013, 2015, 2016) periods. The beginning and ending days of the selected periods and the respective year**s** have

been listed in Table 1. In summary, for the 2013–2016 data set the EO rates are computed over four periods of 42 days each in total, for Autumn and Spring equinoxes, Summer and Winter solstices.

DCE and DCN have been operating simultaneously during 2019 (except for January 2019, since DCN started regular data acquisition from January 28, 2019). The radars transmitting frequency during this period has been 10.9 MHz for DCE and 8.9 MHz for DCN. Analogously to the time intervals selection criteria adopted for the DCE observations during the 2013–2016 years, we chose to consider 14-days periods around equinoxes and solstices for the year 2019. The start and ending days of the four selected periods (one for each season) are listed in Table 2; they were used for both DCE and DCN. The start date of the Spring period is forward shifted by three days with respect to the other intervals due to the presence of data gaps.

The periods under study, listed in Tables 1 and 2, are represented by shaded and hatched areas in Fig. 2. The Winter/Summer periods are indicated by black/grey shadings and the Autumn/Spring periods are indicated by black/grey hatched areas. In this figure, the monthly mean of the International Sunspot Number is reported as a function of time. It can be seen that DCE observations comprised in the statistical data set are for the final part of the maximum of solar cycle XXIV in its descending phase. The DCE and DCN 2019 observations have been performed during the solar cycle minimum.

In this study we also use the electron density at 300 km height derived from the International Reference Ionosphere (IRI) 2016 model (Bilitza et al., 2017) to support the understanding of the EO rates distributions. The IRI model is the empirical climatological model of the ionosphere that is recognized as the official ISO standard for the ionosphere (Bilitza, 2018). IRI provides climatological median values of the electron density, electron and ion temperatures, and ion composition in the ionosphere, on a global basis, for different levels of solar and magnetic activity. In this study, climatological electron density values modeled by IRI (2016 version) at 300 km of height (around the F2-layer peak, i.e., the maximum in the electron density of the ionosphere) are used. The NeQuick topside option (Nava et al., 2008) has been applied for the description of the topside electron density profile shape. Modeled topside electron density values are anchored to the F2-layer peak whose electron density (NmF2) and height (hmF2) have been modeled through the URSI coefficients (Rush et al., 2008) and Shubin et al. (2015) options, respectively. Bottomside F2-layer profile has been modeled through the Altadill et al. (2009) option. It must be noted that monthly median values of the principal ionospheric characteristics, as well as of the whole vertical electron density profile predicted by mod-

Table 1
Time periods considered for the DCE statistical study in the 2013–2016 interval.

Autumn	Spring	Summer	Winter
14-28/03/2013	14-28/09/2013	14-28/12/2014	14-28/06/2013
14-28/03/2014	14-28/09/2014	14-28/12/2015	14-28/06/2014
14-28/03/2016	14-28/09/2016	14-28/12/2016	14-28/06/2016

Table 2
Intervals considered for DCE and DCN in the 2019 year.

Autumn	Spring	Summer	Winter
14-28/03/2019	17/9–01/10 2019	14-28/12/2019	14-28/06/2019

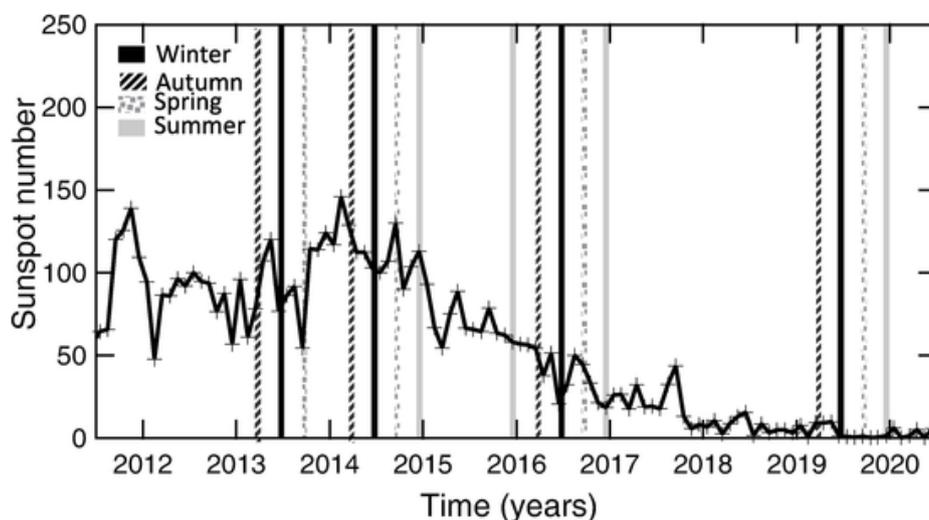**Fig. 2.** Time periods considered in the analysis and the monthly mean values of the International Sunspot Number for the period of 2012–2020. The shadings and hatched areas represent periods considered in the study (as listed in Tables 1 and 2). The Winter and Summerperiod are indicated by dark and grey shadings, respectively. The Autumn and Spring periods are indicated by black and grey hatched areas, respectively.

els, may represent only partially the real conditions of the high-latitude ionosphere (Hunsucker and Hargreaves, 2009). For instance, Themens et al. (2014) found notable differences between IRI and ionosonde *Nm*F2 diurnal and seasonal behavior over the entire period studied, with prevalent errors in excess of 50%, particularly during equinox periods. Concerning *hm*F2, they found that it is marginally overestimated during winter and equinox nighttime, but also underestimated during summer and equinox daytime, with excess of 25%. However, recently several works demonstrated that IRI, although being an empirical climatological model, is much more reliable than most physics-based models in representing the physical conditions of the ionosphere at high latitudes (e.g., Shim et al., 2011, 2012; Tsagouri et al., 2018). Moreover, it has to be considered that the last version (2016) of the IRI model was added with new features, especially for what concerns the *hm*F2 global modeling (Shubin, 2015), that improved the global representation of the vertical electron density profile made by the model. Then, in order to obtain some useful hints for the interpretation of EO occurrence, the choice of the IRI model to characterize the ionosphere electron density background is fully adequate.

3. DCE ionospheric and ground scatter rates patterns for equinoctial and solstice periods

We present the results of the DCE EO computation for the 2013–2016 interval in Fig. 3 while the results for the 2019 periods are shown in Fig. 4. The 2013–2016 EO rates (Fig. 3) pertain to the operating frequency of 10.3 MHz while the 2019 rates (Fig. 4) pertain to the operating frequency of 10.9 MHz. The two figures have the same format. In the left/right column, the polar maps of the IS/GS rates values computed for each of the MLT-MLAT cells are shown, from top to bottom, for the Autumn, Spring, Summer, and Winter periods of the reference interval. Noon MLT is at the top of the maps, dawn (6 MLT) is to the right and dusk (18 MLT) is to the left. The EO ratios are expressed in percent (the ratio value one corresponds to 100) and represented by a logarithmic colour scale. In order to interpret the features of the IS rate maps, contours of the MLT-MLAT average electron density at 300 km are overplotted on the maps. The average electron density was derived from the electron density distribution as given by the IRI-2016 model using the following procedure. We choose a reference day for each (of 8) data set. For the 2013–2016 data set, the four equinoxes and solstices days in 2013 were considered. For the 2019 periods we considered the days corresponding to March 21, 2019, June 21, 2019, September 24, 2019, and December 15, 2019. For each of the reference days, we computed the IRI electron density values at 300 km height (hereinafter we would simply say "electron density") for each beam-range cell of the DCE FoVs at 10 min UT time intervals. Afterwards, all such values are binned in 20 min MLT x 2° MLAT pixels and then averaged. When considering such beam-averaged electron density maps, it must be kept in mind that only one day for each period is considered for the computation of the electron density. This is acceptable for the 2019 periods, since the IRI electron density variation over days is small. For the 2013–2016 periods, the electron density maps are derived from equinoxes and solstices of the year 2013, therefore the maps are a rough representation of the electron density for the longer periods of interest (including equinoxes and solstices also for years 2014, 2015 and 2016). On the other hand, the procedure takes into account the fact that the illumination, and therefore in the first approximation the relative electron density in each beam-range cell, is different from each other over a day. Consequently, we believe that the obtained maps can indeed be used for qualitative comparisons and reasoning.

Several features can be noted in the IS rates patterns for the 2013–2016 data set (left column of Fig. 3):

1. The IS rate patterns for the Autumn and Spring equinoxes (two upper panels) are similar. At small distances from the radar, within
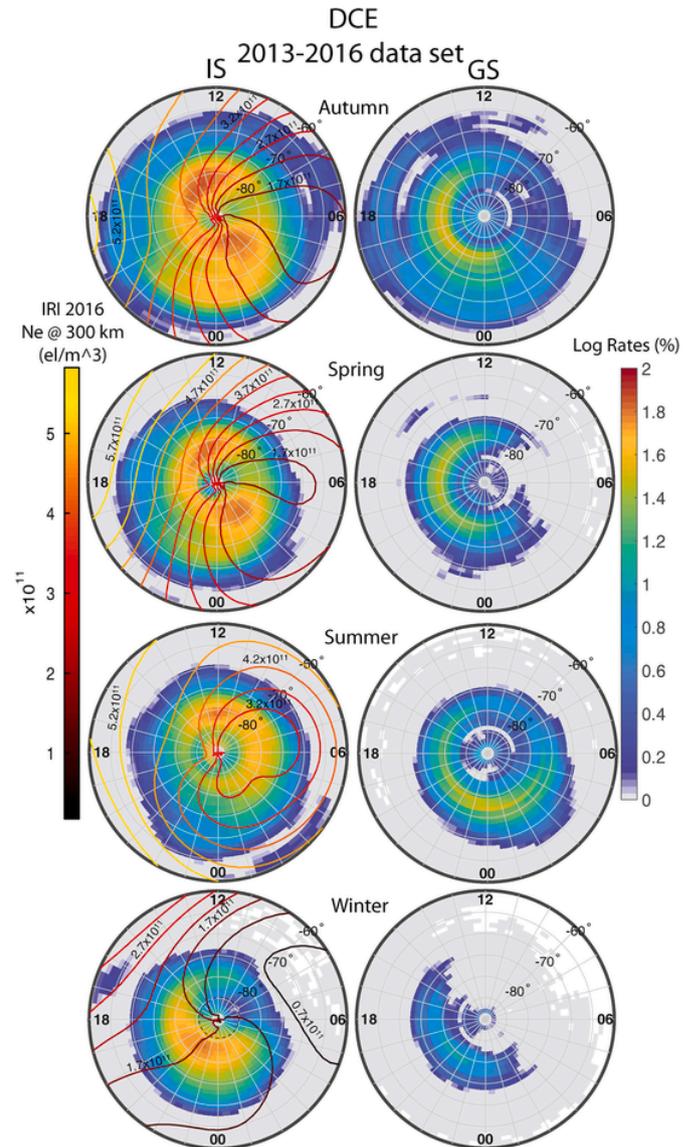

Fig. 3. Dome C East ionospheric scatter (IS), left column, and ground scatter (GS), right column, Echo Occurrence (EO) rates for the 2013–2016 dataset plotted in MLT- MLAT coordinates. The maps from top to bottom are for Autumn, Spring, Summer and Winter, respectively. The GS rate maps are for the same periods. Noon MLT is at the top of the maps, dawn (6 MLT) is to the right and dusk (18 MLT) is to the left. The EO rates are expressed as logarithm of percents (the rate of 1 corresponds to 100 percent) according to the logarithmic colour scale on the right. The contours of the beam averaged electron density at 300 km are overplotted on the IS maps. The contours are coloured according to the scale on the left of the figure. The electron density is derived from the IRI-2016 model for equinoxes and solstices of 2013 as described in the text. (For interpretation of the references to colour in this figure legend, the reader is referred to the Web version of this article.)

the −85° MLAT circle, the IS rates are homogeneous and the EO rate is about 25%. The rates in the belt of −85° - −70° MLAT shows an "S" shape pattern with asymmetric dayside and nightside parts. Such pattern consists of: two regions of enhanced rate (65%) centered at about 1330 and 0230 MLT (at approximately −82° MLAT), connected by a narrower region of lower rates at about the same latitude in the afternoon sector; a region of slightly enhanced rates (34%) in the 21 - 03 MLT sector at about −75° MLAT; a low rates region between 05 and 08 MLT. This low rate region is well delimited by the 1.7×10^{11} m^{-3} contour of the 300 km electron
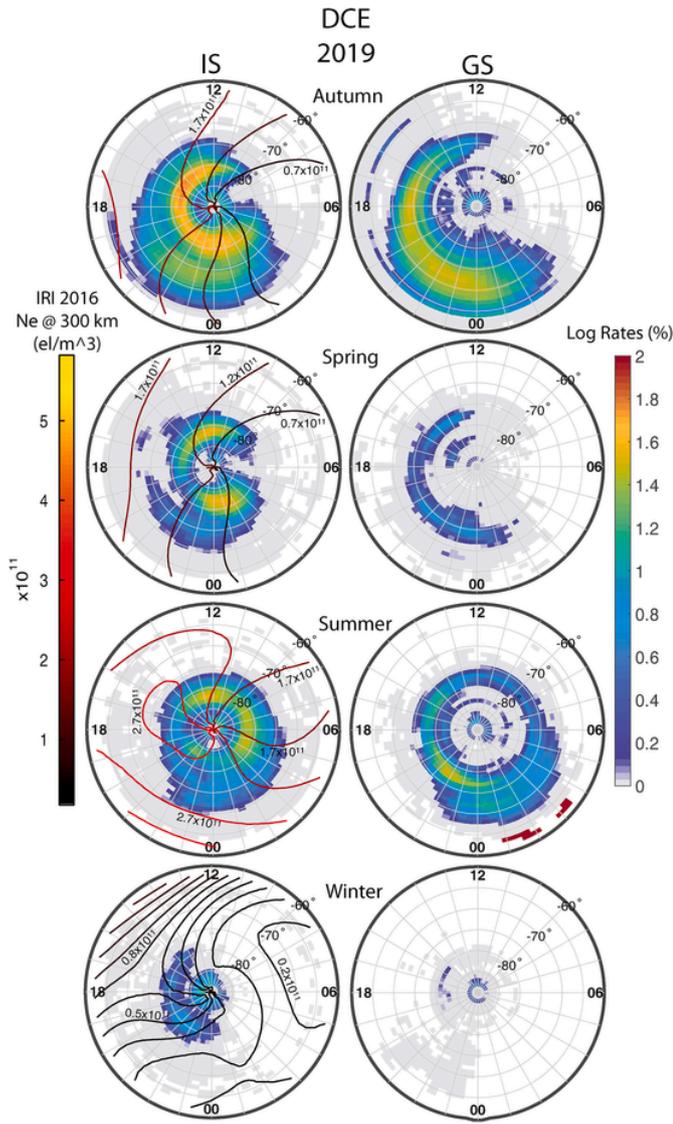
Fig. 4. The same as in Fig. 3 but for Dome C East observations in 2019. The average electron density overplotted on the IS rates is derived from the IRI-2016 model electron density values at 300 km on March 21, 2019 (Autumn equinox period), June 21, 2019 (Winter solstice period), September 24, 2019 (Spring equinox period), and December 15, 2019 (Summer solstice period).

density. The IS rates are very low for latitudes below −70°. The IS rates are slightly lower in Spring than in Autumn.

2. The Summer solstice IS rate pattern (third panel) is different from that at the equinoxes. At small distances from the radar, within −85° MLAT circle, the IS rate is slightly enhanced in the afternoon with respect to dawn. The rates in the belt of −85° - −80° MLAT show an enhancement region (56%) at noon. In this belt, the 16–22 MLT sector shows low IS rates (26%). The IS rates sharply decrease at latitudes below −80°, and there is a tendency for IS to occur at slightly lower latitudes on the night side with respect to the dayside.

3. The Winter solstice IS rates pattern (bottom panel) is different from both the equinoxes and the Summer solstice cases. Moderately enhanced rates are only visible in the afternoon/midnight 18 - 02 MLT sector, between approximately −85° and −80° MLAT. The low rates region in the 04–13 MLT sector is well delimited by the $1.2 \times 10^{11}\ m^{-3}$ contour of the electron density.

As far as the GS rates are concerned (right column), the Spring and Autumn distributions are similar with a belt of enhanced values in between −75° and −80° MLAT in the dusk sector. In Summer, a similar enhanced GS rates belt is present. In this case, the belt extends all around from 12 MLT to 5 MLT. In Winter, the GS rate is drastically reduced and it is only present around 21 MLT at −82° MLAT.

We now describe the results obtained for the 2019 interval, Fig. 4. The IS rates for the equinoctial and solstice periods show patterns that are similar to the ones of the corresponding periods in the 2013–2016 data. The main difference between the IS rates of the two intervals is in their overall values, with the rates in 2019 being generally lower than those in 2013–2016. In 2019, the maximum rate value was registered at about 1530 MLT in Autumn and it is about 55%. The IS rate is drastically reduced in the 2019 Winter, with a maximum value of about 7% at 21 MLT. It can also be noted that the rates within the −85° MLAT circle show slightly enhanced values in the dawn (dusk) sector in the equinoctial periods and Summer solstice (Winter solstice). The IS rates are lower in Spring than in Autumn, as for the 2013–2016 dataset. It can be seen that the electron density is lower than that in the 2013–2016 interval as well. Comparing the IS rates pattern with the electron density distribution, one can see that the $0.7 \times 10^{11}\ m^{-3}$ electron density contour level delimits the region of IS rates absence for the equinoctial periods. In Winter, echo occurrence is non-zero for electron density values greater than $0.4 \times 10^{11}\ m^{-3}$. The GS rates patterns are similar to the ones of the 2013–2016 interval, except that the GS occurrence regions are shifted to lower latitudes. The GS occurrence rate values are, overall, lower in 2019 as compared to those in 2013–2016, except for the Autumn period.

4. DCN ionospheric and ground scatter rate patterns for equinoctial and solstice periods in 2019

The EO analysis results for the new DCN radar are presented in Fig. 5 in the same format as that in Figs. 3 and 4. The DCN radar operating frequency in 2019 was 8.9 MHz. The electron density distribution pattern is different here which comes from the fact that, as already mentioned, the DCN and DCE FoVs are differently illuminated.

1. The IS rate patterns for the Autumn and Spring equinoxes (two upper panels) are similar. At small distances from the radar, within approximately the −85° MLAT circle, the IS rates have slightly higher values in the 18-00 MLT sector. The rates of the belt in the −85° - −75° MLAT interval are enhanced between 12 and 02 MLT. The IS rates for Autumn are higher than in Spring. The regions characterized by the lowest rates in both equinoctial periods are approximately delimited by the $0.7 \times 10^{11}\ m^{-3}$ contour of the electron density. The IS rates are very low and echoes are almost absent for latitudes below −75°.

2. The Summer solstice IS rates pattern (third panel) differs from the equinoxes' pattern. At small distances from the radar, within the −85° MLAT circle, the IS echoes are almost absent. The rates at −85° - −80° MLAT are generally low except for an enhanced values region (52%) at noon. The IS rates sharply decrease for latitudes below −80°. Nevertheless, it can be noted that IS rates decrease abruptly in the dawn sector and more slowly elsewhere, with IS echoes observed at slightly lower latitudes on the night side as compared to the dayside.

3. The Winter solstice IS rates pattern (bottom panel) is different from both the equinoxes and Summer solstice periods. The IS is practically absent in the 17 - 07 MLT sector. IS rates are rather high in the MLT sector centered at 12 MLT. The region where echoes are absent is delimited by the $0.7 \times 10^{11}\ m^{-3}$ contour of the electron density.

As far as the GS rates are concerned (right column), the highest rates are observed for Autumn. For all other periods the GS rates are very low.
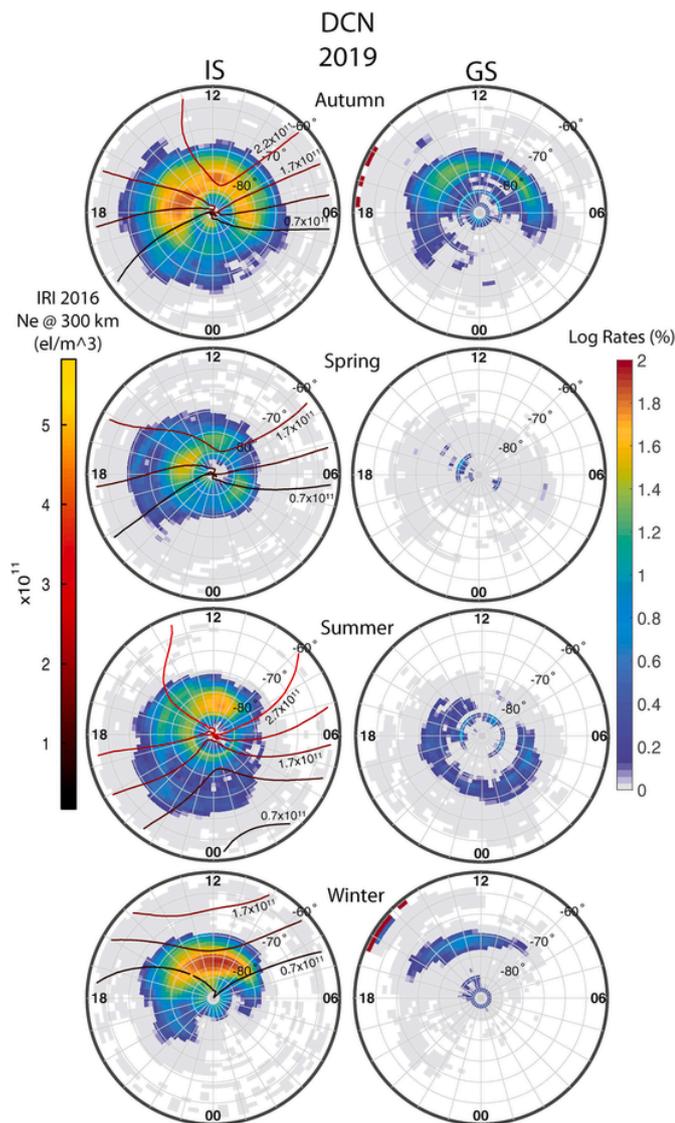
Fig. 5. The same as in Fig. 4 for the Dome C North radar.

5. DCE IS rates levels and their dependence on radar transmitting frequency and auroral activity

Echo occurrence dependence on the frequency of the radar transmissions and on the level of the geomagnetic activity has been observed in SuperDARN radar data (e.g. Milan et al., 1997). To illustrate the dependence of the DCE IS rates on both the signal frequency and on the geomagnetic activity, we categorize the seasonal data sets according to the operating frequencies and the AE index. The choice of the AE index (instead of e.g. the planetary Kp index) is based on the fact that the auroral current system plays the major role in affecting the polar region monitored by DCE. Although the AE index is the most appropriate to monitor the effects of the magnetospheric dynamics in the polar and high latitudes ionosphere, it has the drawback that it is computed from geomagnetic field measurements performed by a network of observatories in the Northern Hemisphere, while it is known that hemispheric differences exist in the auroral precipitation. Indeed, Luan et al. (2010) found that the auroral hemispheric power shows inter-hemispheric differences of about 20% during quiet conditions and a more symmetric situation is observed during moderate and active conditions. Unfortunately, a Southern AE index is not available for a number of reasons, among which is the unfavorable distribution of land and sea at the high Southern latitudes. Relying on a certain degree of connection between

the Northern and Southern Hemisphere phenomena, observations relative to one Hemisphere have been often used in the study of the other Hemisphere phenomena (e.g. Lockwood et al., 2006). We proceed analogously. As far as the classification based on AE index is concerned, we define two different geomagnetic activity levels as characterized by AE < 80 nT (AE Low) and AE > 100 nT (AE High). Afterwards, we compute the MLT-MLAT maps for the Frq1 ($\simeq$ 10 MHz) and Frq2 ($\simeq$ 12 MHz) frequencies and the two different magnetic activity levels. We then integrate the maps values of the IS rates over MLT to infer auroral activity effects as a function of magnetic latitude. In addition, this kind of representation also permits to better assess the seasonal differences in the overall level of the IS rates, since the colour maps are most effective for highlighting the rates patterns, while the examination of the magnetic latitude profiles allows to better compare the IS rates quantitatively. It is important to keep in mind that as the distance from the DCE and DCN radars increases the MLAT of echo detection decreases.

Results are displayed in Fig. 6. At equinoctial periods a maximum rate of about 60% (65% for the Autumn equinox) is found approximately at −82° MLAT. Then the rate smoothly decreases. For the Spring equinox it becomes very small by −65° MLAT. The Autumn equinox rate shows very low values down to the lowest latitudes reached by the radar FoV, when the radar operated with 100 range gates. The smooth decrease from high to low latitudes is an effect of the integration in all MLT hours. In fact, two peaks are observed, for example, when limiting the integration to the midnight sector hours (not shown). At solstices the peak in the IS rate is lower and is found at lower latitudes with respect to the equinoctial cases, especially for the Winter case. For the Summer case a second peak is evidenced (better than in the map representation) at very high latitudes (small distances from the radar). The frequency effect can be clearly seen for all the four seasons. The Frq2 IS rates are overall lower than the Frq1 IS rates. In particular, the Frq2 IS rate is much lower than Frq1 IS rate at latitudes above −75° MLAT. In Summer, for example, the Frq2 IS rate peak is reduced to half the value of the Frq1 IS peak. Also, the rates peak positions are different in the equinoctial and Summer solstice periods, being the Frq2 peak at lower latitudes (that is at larger distances from the radar).

As far as the AE dependence is concerned, this is again visible in all the different seasons and for both Frq1 and Frq2. In the Equinoctial periods, the AE Low and AE High rates are generally similar for latitudes above −78° MLAT, while the AE High rates are larger than the AE Low rates in the −78° - −67° MLAT interval. Interestingly, for Frq1 the AE Low rates go over the AE High rates for latitudes lower than about −67° MLAT. In Summer, the AE High rates are larger than AE Low rates for latitudes above −83° MLAT, in correspondence of the IS rates second peak, and for latitudes lower than −78° MLAT; the AE Low rates are similar to the AE High rates for latitudes in the −78° - −82° MLAT interval. In Winter, the AE High rates are generally greater than the AE Low rates. The largest differences between AE High and AE Low rates occur at about −75° MLAT and at this latitude such differences are largest for Frq1.

6. Discussion

The patterns of the DCE EO rates in the MLT-MLAT maps show a great seasonal variability. Such variability is likely related to the variability of the ionospheric electron density. The relationship between EO and ionospheric electron density has been already reported (Ruohoniemi and Greenwald, 1997; Koustov et al., 2004; Kane et al., 2012; Ghezelbash et al., 2014a, 2014b; Lamarche and Makarevich, 2015) and extensively studied in Koustov et al. (2019). Comparison of the DCE IS from the F region and the beam averaged electron density at 300 km, derived from the IRI-2016 model, shows that the regions with strongly reduced DCE IS rates, or where a complete absence of echoes is registered, are associated with the electron density lower than 10^{11} m^{-3}. This result is qualitatively consistent with the finding, ob-
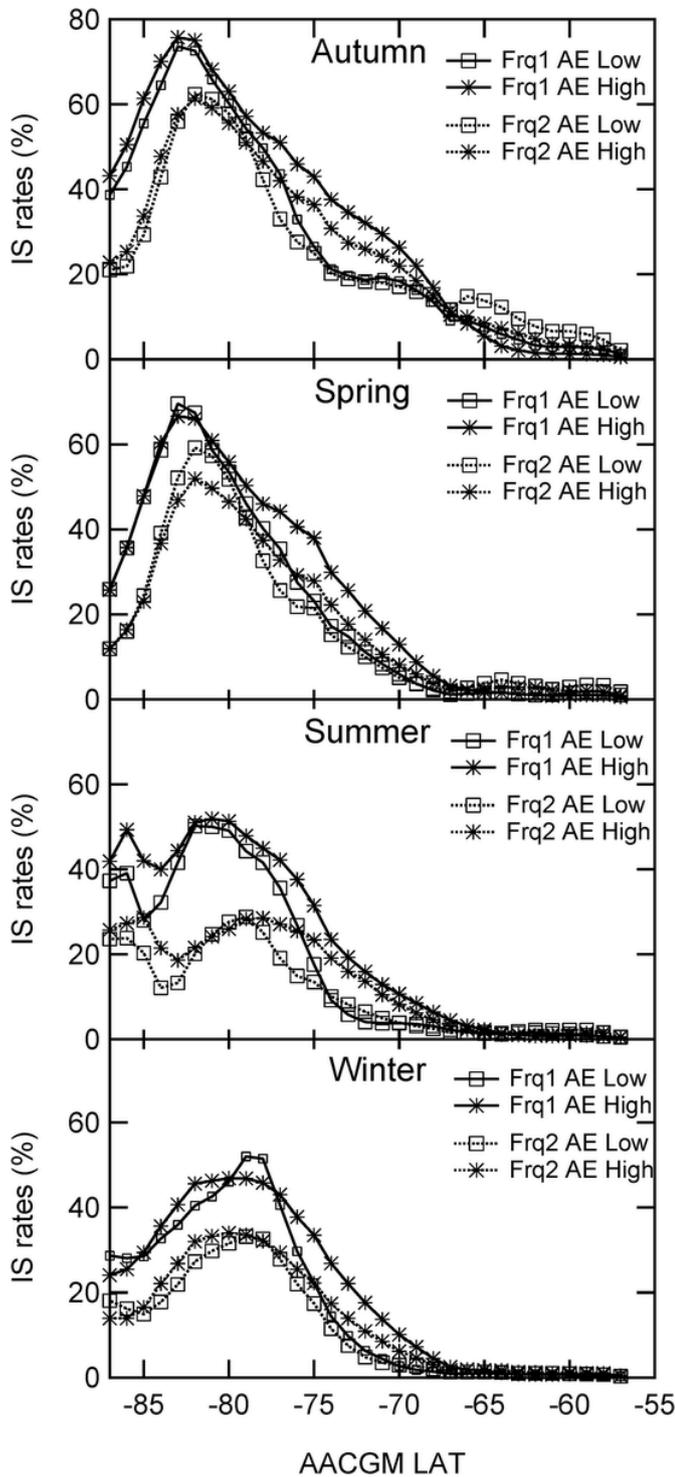
Fig. 6. Dome C East ionospheric scatter occurrence rate versus magnetic latitude for observations at different radar operating frequencies and levels of auroral activity. The plots from top to bottom are for Autumn, Spring, Summer and Winter periods, respectively. The IS rates for observations at operating frequency Frq1 $\simeq$ 10 MHz and Frq2 $\simeq$ 12 MHz are represented by black solid and dashed lines, respectively. The star and the square symbols are used to represent data for the AE-High and AE-Low subsets, respectively.

tained by means of the comparison with both direct and indirect measurements of the electron density, that the typical threshold for Super-DARN echo detection is close to $2 \times 10^{11}\ m^{-3}$ (Koustov et al., 2014, 2018, 2019). It is also evident that the DCE IS occurrence rates are reduced in 2019 as compared to those in 2013–2016. This can be again

related to the corresponding decrease in the electron density as predicted by the IRI-2016 model and this confirms the conclusion by Koustov et al. (2019) that the electron density has a major role in determining the overall SuperDARN polar cap echo occurrence reduction in the descending phase of the solar cycle XXIV. Moreover, an Autumn-Spring asymmetry is present both in the DCE 2013–2016 dataset and in the 2019 DCE and DCN datasets, where the IS rates values in Autumn are higher than in Spring. This also could be related to equinoctial asymmetries in the electron density, with higher values in Autumn than in Spring, a phenomenon that has been observed principally at low latitudes (e.g. Liu et al., 2010), but also in the polar cap (e.g. Hatchet al., 2020). In the Summer dataset of the 2013–2016, the DCE IS rate is generally lower with respect to the equinoctial observations, despite the higher electron density. As suggested by Koustov et al. (2019), an explanation for this could be based on the effect of smoothing of the plasma density gradients under long periods of solar illumination (up to 24 h) and consequently diminished production of irregularities through the gradient-drift plasma instability, which is considered the most important mechanism for irregularities generation (Ossakow and Chaturvedi, 1979; Tsunoda, 1988). This could also be due to an increased electron density in the D and E regions causing enhanced HF signal absorption (Ruohoniemi and Greenwald, 1997; Ghezelbash et al., 2014a). It is interesting to note that the largest IS rates in the 2013–2016 Summer pattern, not taking into consideration the IS rate maximum occurring at 12 MLT, correspond to the regions of lower electron density. At the same time, the afternoon/midnight sector around 20 MLT shows lower IS rates. Actually, as already mentioned in Sections 3 and 4, a similar IS depletion is present around 20 MLT in the equinoctial maps as well. Such depletion concurs with the presence of IS scatter at lower latitudes in the afternoon/midnight sector, giving the peculiar "S" shape to the equinoctial IS rate patterns.

With the aim of understanding the causes of these features in the MLAT-MLT maps, we make a comparison between the DCE EO and ray tracing simulations. We concentrate on the 12 MLT, 20 MLT and 00 MLT sectors for the Autumn equinoctial period of 2013–2016. The ray tracing results are reported in the upper panels of Fig. 7. We used a set of ray tracing tools based on numerical solutions of the Hamiltonian ray path equations (Haselgrove, 1963; Jones and Stephenson, 1975) which allows the introduction of arbitrary density distributions. In particular, for our simulation we used the IRI-2016 model densities on March 21, 2013. The ray tracing is done for the beam 8 of DCE at 20 UT, 04 UT and 08 UT, when the considered beam was aligned with the three MLT meridians under study. The elevation angles are comprised in the 0°–30° interval. The simulations are run for a frequency of 10.4 MHz, that is for the Frq1 case. In the ray tracing plots (Fig. 7, panel a), the electron density is colour coded, the geomagnetic field lines are represented by yellow segments, and rays are represented by white lines. Along each ray path, magenta points identify ray segments for which the orthogonality condition with the geomagnetic field is satisfied within $\pm 0.5°$. In other words, the magenta segments represent predicted ionospheric backscatter loci in the case electron density irregularities are present. When the density is such that refraction bends the rays towards the Earth surface, ground or sea scatter can occur, depending on the roughness of the surface itself. Ray tracing results are shown as a function of the distance from the radar site. According to the ray tracing results for the 12 MLT and 00 MLT, the IS scatter coming from $\frac{1}{2}$ F hop and $1\frac{1}{2}$ F hop could be detected by DCE; 1 hop and 2 hop rays are scattered back to DCE from the Earth surface, although the 2 hop is back scattered far away from the radar (at distances larger than 2800 km). Ionospheric $\frac{1}{2}$ F hop and $1\frac{1}{2}$ F hop, and Earth surface 1 and 2 hop ground scatter could be registered for 20 MLT. In the DCE case, scatter from the Earth surface is most probably coming from the sea, since the icy surface of the Antarctic plateau underneath the DCE FoV is too smooth to back scatter the rays (Ponomarenko et al., 2010).
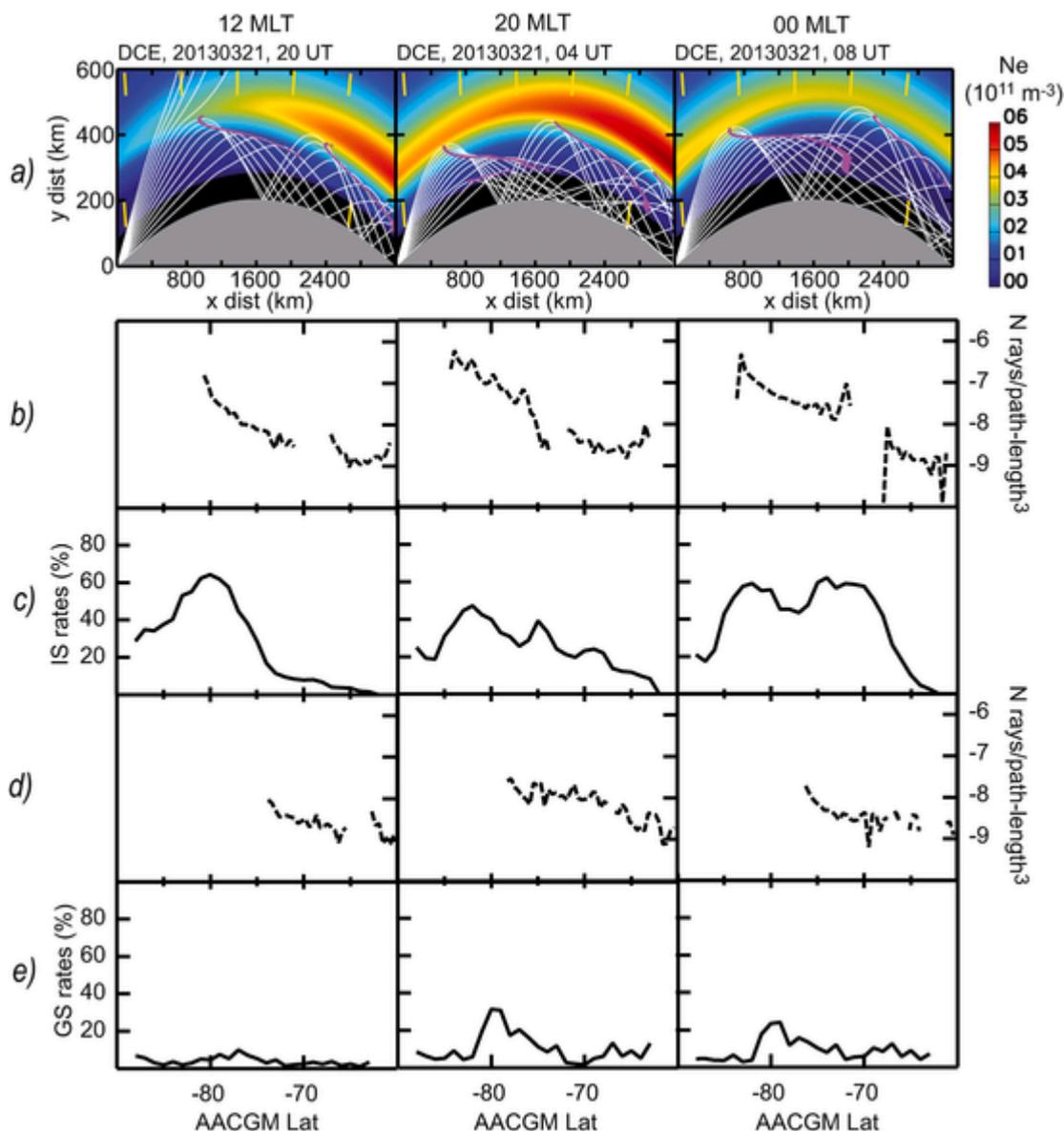
Fig. 7. Ray tracings for the Dome C East radar beam 8 for 12 MLT, 20 MLT and 00 MLT of the Autumn equinoctial period of 2013–2016. The electron density distribution was taken according to the IRI-2016 model on March 21, 2013. It is represented by the colour according to the scale shown on the right of the top row. Yellow segments indicate the geomagnetic field lines orientation. Rays are shown by white lines. Along each ray path, magenta points identify ray segments for which the orthogonality condition with the geomagnetic field lines is satisfied within $\pm0.5°$. Ray tracing results are shown in terms of the distance from the radar site. Panels in row b) are the expected ionospheric signal strength for the respective ray tracings (strength is characterized by the number of rays within each 45 km path-length bin that satisfy the orthogonality condition weighted by the $1/r^3$ factor, where r is the path-length). Panels in row c) are ionospheric echo occurrence rates for the Dome C East radar at the three MLT sectors considered in modelling. Panels in row d) are the same as in b) but for ground scatter. Panels in row e) are the same as in c) but for ground scatter (only the $1/r^3$ factor was considered). (For interpretation of the references to colour in this figure legend, the reader is referred to the Web version of this article.)

The plots of the panels from b) to e) of Fig. 7 present a more explicit comparison between the DCE EO and the ray tracing results. The IS and GS rates profiles along the three MLT meridians under study are reported in c) and e). Similarly to de Larquier et al. (2013), we compute the number of rays that satisfy the orthogonality condition or that reach the ground after refraction in the ionosphere falling into each 45 km path-length bin. The path-length r of a ray is the length of the ray from the radar to the scatter region. The counts are then weighted by $1/r^3$ to take into account the geometric power decay ($1/r^4$) and considering the compensation due to the linear increase of the scattering region size. In b) and d) the weighted counts are reported as a function of MLAT for the ionospheric scatter and ground scatter, respectively. The results shown in b) and d) give only an indication on where the ionospheric or ground scatter can be generated, but the actual echo detection

levels depend on the presence of the irregularities, for the IS, and on the surface characteristics, for the GS. We note that, as opposed to de Larquier et al. (2013), we do not multiply the weighted counts for the squared electron density, to which the amount of irregularities should be proportional (see Ponomarenko et al., 2009). When using this factor, it is assumed that the irregularities distribution is uniform. We prefer not to make any assumption and use a homogeneous representation of the IS and GS ray tracing predictions. We also note that the EO has been derived from a statistical dataset, while the simulation is run for a specific beam and for the Autumn equinox of 2013. However, from the comparison between the EO and the IS and GS characterization by ray tracing some conclusions can be drawn that help in understanding the origin of the IS patterns. The observed IS peak at $-80°$ MLAT and 12

MLT seems to correspond to the $\frac{1}{2}$ F hop predicted by the ray tracing. No echo occurrence was registered contrary to the predicted $1\frac{1}{2}$ F hop signals. The observed 12 MLT GS is very low and shows slightly higher values at about −78° MLAT. The predicted GS peak is located at about −75° MLAT. The observed IS at 20 MLT shows a peak at about −82° MLAT and then a slow decrease at lower latitudes, with two relatively low peaks at −74° and −68° MLAT. The observed IS seems to originate from the predicted $\frac{1}{2}$ F and $1\frac{1}{2}$ F hop, which are separated by few degrees in latitude at about −73° MLAT. The observed 20 MLT GS shows a peak at about −80° MLAT with a slow decrease towards lower latitudes and it is congruent with the predicted GS that, however, does not show any prominent peak.

The IS observed at 00 MLT shows enhanced values in the −84° to −67° MLAT interval with two relative peaks at −82° and −72° MLAT: it seems to correspond to the predicted $\frac{1}{2}$ F hop, that extends from −85° to −71° MLAT. Similarly to the 12 MLT case, no IS echo occurrence is registered in correspondence of the predicted $1\frac{1}{2}$ F hop. The observed GS shows a peak at about −80° MLAT with a slow decrease towards lower latitudes which can be associated with the predicted 1 hop GS.

In summary, the IS occurrence at lower latitudes for the 20 MLT and 00 MLT sectors seems to be due to the particular propagation conditions in the afternoon/midnight sector. For the 00 MLT, the IS depletion seems to be related to a lower number of rays meeting the orthogonality condition. Moreover, at 12 MLT electron density is not high enough to bend the high elevation angle signals and only part of the radar waves is refracted in the ionosphere. Correspondingly, the amount of signal that can be back scattered from the Earth surface is diminished and occurs at lower magnetic latitudes. At 20 MLT and 00 MLT, electron density is high enough for all the rays to be refracted and the IS starts at higher latitudes. Correspondingly, the rays that reach the surface are more numerous so that the GS is favoured and occurs at higher latitudes, as well. A strong GS signal can mask the IS detection (e.g. Milan et al., 1997). Therefore, the depletion of IS scatter observed at about −80° MLAT can be also due to the occurrence of the GS, that is observed and predicted by the ray tracing simulations. Koustov et al. (2019) already suggested that such an effect could play a role in the modulation of the IS occurrence in the Southern polar cap radar observations at the noon local time. Therefore, the above considerations give an indication that the "S" shape of the equinoctial DCE patterns is due to the particular ray propagation determined by the electron density distribution. The GS masking effect can be at work during the Summer solstice periods as well. In fact, GS is observed in the afternoon/midnight sector of the Summer GS maps of Fig. 3, where the IS reduces. Otherwise, a less IS occurrence at lower latitudes is registered, probably because the horizontal electron density distribution is different with respect to the equinoctial periods, so that the Summer distribution has not the peculiar "S" shape characterizing the equinoctial patterns.

We look at the ray tracing results also for the 07 MLT (not shown). It appears that the electron density is too low to sufficiently bend the radar signals, consequently the majority of the HF waves is not refracted and does not meet the orthogonality condition. Therefore, unfavorable propagation conditions could play an important role in the reduction of the DCE echoes detection around the 07 MLT sector.

Regarding the overall consistency between the EO occurrence and the ray-tracing simulations, it is worth to mention that the same consistency is not found when the IRI-2012 version is used as the background model for the electron density. In particular, the ray tracing results based on IRI-2012 (not shown) predict that the first IS backscatter occurs at significant lower latitudes than the observed ones.

Looking now at the DCN EO observations, the IS and GS rates patterns are completely different from the DCE ones in terms of MLT and MLAT distributions, as it has been described in Section 4. However, when all the features present in DCE and DCN patterns are considered

with respect to the electron density distribution a high level of similarity is evident. The different illumination of the two radars FoVs is such that the IS occurrence in DCN MLT-MLAT regions are complementary to the DCE ones. Despite the patterns similarities in terms of electron density distribution, the DCN IS rates from the F region are overall higher than the DCE IS rates. This could be related to the fact that the DCN operating frequency during the periods under study was lower than the DCE frequency. It is suggested that a decrease in frequency could increase the IS (e.g. Milan et al., 1997). This effect is also clearly observed for DCE, as shown in Fig. 6.

Concentrating on the IS scatter at near ranges gates, which is likely the IS from the E region, it can be observed that for the equinoctial periods of both the 2013–2016 DCE dataset and the 2019 DCE and DCN datasets a slightly enhanced IS rate is observed in regions where high electron density gradients can be present, specifically at about 11 MLT and 01 MLT sector for DCE and 21 MLT sector for DCN. An enhancement of the E region IS is also visible in the afternoon sector for the 2013–2016 Summer solstice. In this case, the electron distribution seems to be characterized by electron density gradients. We speculate that this could be due to the "grey ionosphere" effect in which the non uniformity of electron density favours ray propagation and irregularities production (Ghezelbash et al., 2014a). However, such a mechanism has been taken into consideration for the F region IS. Moreover, the role of density gradients is considered of less importance in the polar cap (Forsythe and Makarevich, 2015, and references therein).

The results presented in this study can be explained, at least qualitatively, in terms of the electron density variability over the solar cycle, season, and day. Indeed, the DCE IS rates do not show a strong variability between different levels of auroral activity. This can be partly due to the peculiarity of the solar cycle XXIV progression. It must be noted, however, that a quantitative assessment of possible effects due to other processes related, for example, to the interaction between the solar wind and the magnetosphere has not been performed in the present study. Finally, it is interesting to note that the regions of enhanced IS rates for the 2013–2016 DCE and 2019 DCN datasets in the Summer solstice are observed to correspond to the geomagnetic cusp.

7. Conclusion

In the present study, the maps of the ionospheric and ground scatter echo occurrence rate for the Southern radars DCE and DCN were presented in MLT-MLAT coordinates for equinoctial and solstice periods. The dataset examined for DCE comprised twelve 14-day long periods, three for each equinox and solstice, from the 2013 to 2016 and four 14-day long periods for the equinoxes and solstices of the year 2019. For the same 2019 periods, echo occurrence rates for the new DCN radar were also presented. DCE and DCN are both located near the Southern geomagnetic Pole and their FoV are almost aligned with the magnetic meridians. Despite such a symmetry in terms of the geomagnetic locations monitored, the DCE and DCN EO patterns on the MLT-MLAT maps showed great differences and large variability with season. This is very likely due to the fact that the radars' FoV are exposed differently to solar illumination over a day and with the season progression. In fact, the DCE and DCN echo occurrence patterns on the MLT-MLAT maps can be explained by the variation in the electron density in the ionosphere affecting the radars signal propagation conditions. In terms of the sounding efficiency of the key regions for the magnetospheric dynamics monitoring, it is found that the DCE back scatter rates are often above 50% in significant portions of the polar cap, notwithstanding that the dataset pertains to the descending phase of the solar cycle. DCN IS rates are also high on the dayside, especially considering that the dataset under examination pertains to the solar cycle minimum. Importantly, the DCE and DCN coverages are complementary in terms of the MLT sectors. This study shows that DCE and DCN radars in combination are capable of receiving IS in extended, but not overlapping

MLT sectors and thus they provide more even, in terms of the coverage, monitoring of the Southern polar cap area. Our observations confirm that the echo detection rate increases as the operating frequency decreases from 12.3 MHz to 10.4 MHz. Currently, the DCE and DCN operating frequencies are 10.9 MHz and 8.9 MHz, respectively. With this choice, good echo rates are highly expected for the coming years. A more quantitative comparison between DCE and DCN data and the ray tracing simulations will be performed in future studies in order to understand the complex interplay between the physical processes at work in the polar cap and high latitude ionosphere and HF radar capabilities in their monitoring.

Declaration of competing interest

The authors declare that they have no known competing financial interests or personal relationships that could have appeared to influence the work reported in this paper.

Acknowledgments

References

Altadill, D., Torta, J.M., Blanch, E., 2009. Proposal of new models of the bottomside B0 and B1 parameters for IRI. Adv. Space Res. 43, 1825–1834. https://doi.org/10.1029/2003JA010307.

Bilitza, D., 2018. IRI the international standard for the ionosphere. Adv. Radio. Sci. 16, 1–11. https://doi.org/10.5194/ars-16-1-2018.

Bilitza, D., Altadill, D., Truhlik, V., Shubin, V., Galkin, I., Reinisch, B., Huang, X., 2017. International Reference Ionosphere 2016: from ionospheric climate to real-time weather predictions. Space Weather 15. https://doi.org/10.1002/2016SW001593.

Bristow, W.A., Spaleta, J., Parris, R.T., 2011. First observations of ionospheric irregularities and flows over the South geomagnetic pole from the super dual auroral radar network (SuperDARN) HF radar at McMurdo station, Antarctica. J. Geophys. Res. Space Phys. 116, A12325. https://doi.org/10.1029/2011JA016834.

Chisham, G., Lester, M., Milan, S.E., Freeman, M.P., Bristow, W.A., Grocott, A., McWilliams, K.A., Ruohoniem, M.J., Yeoman, T.K., Dyson, P.L., Greenwald, R.A., Kikuchi, T., Pinnock, M., Rash, J.P.S., Sato, N., Sofko, G.J., Villain, J.P., Walker, A.D.M., 2007. A decade of the super dual auroral radar network (SuperDARN): scientific achievements, new techniques and future directions. Surv. Geophys. 28, 33–109. https://doi.org/10.1007/s10712-007-9017-8.

Chisham, G., Yeoman, T.K., Sofko, G.J., 2008. Mapping ionospheric backscatter measured by the SuperDARN HF radars—Part 1: a new empirical virtual height model. Ann. Geophys. 26, 823–841. https://doi.org/10.5194/angeo-26-823-2008.

Danskin, D.W., Koustov, A.V., Ogawa, T., Nishitani, N., Nozawa, S., Milan, S.E., Lester, M., Andre, D., 2002. On the factors controlling the occurrence of F-region coherent echoes. Ann. Geophys. 20, 1399–1413. https://doi.org/10.5194/angeo-20-1385-2002.

Forsythe, V.V., Makarevich, R.A., 2015. Dual radar investigation of e region plasma waves in the southern polar cap. J. Geophys. Res. 120, 9132–9147. https://doi.org/10.1002/2015JA021664.

Ghezelbash, M., Fiori, R.A.D., Koustov, A.V., 2014a. Variations in the occurrence of SuperDARN F region echoes. Ann. Geophys. 32, 147–156. https://doi.org/10.5194/angeo-32-147-2014.

Ghezelbash, M., Koustov, A.V., Themens, D.R., Jayachandran, P.T., 2014b. Seasonal and diurnal variations of PolarDARN F region echo occurrence in the polar cap and their causes. J. Geophys. Res. Space Phys. 119, 10426–10439. https://doi.org/10.1002/2014JA020726.

Greenwald, R.A., Baker, K.B., Dudeney, J.R., et al., 1995. DARN/SuperDARN. Space Sci. Rev. 71, 761–796. https://doi.org/10.1007/BF00751350.

Haselgrove, J., 1963. The Hamiltonian ray path equations. J. Atmos. Terr. Phys. 25, 397–399. https://doi.org/10.1002/2015JA021664.

Hatch, S.M., Haaland, S., Laundal, K.M., Moretto, T., Yau, A., Bjoland, L.M., et al., 2020. Seasonal and hemispheric asymmetries of F region polar cap plasma density: swarm and CHAMP observations. J. Geophys. Res.: Space Phys. 125, e2020JA028084. https://doi.org/10.1029/2020JA028084.

Hosokawa, K., Nishitani, N., 2010. Plasma irregularities in the duskside subauroral ionosphere as observed with midlatitude SuperDARN radar in Hokkaido. Radio Sci. 45, RS4003. https://doi.org/10.1029/2009RS004244.

Hunsucker, R.D., Hargreaves, J.K., 2009. The High Latitude Ionosphere and its Effect on Radio Propagation. Cambridge University. Press, Cambridge.

Jones, R.M., Stephenson, J.J., 1975. A versatile three-dimensional ray tracing computer program for radio waves in the ionosphere. J. Atmos. Terr. Phys. 25, 397–399.

Kane, T.A., Makarevich, R.A., Devlin, J.C., 2012. HF radar observations of ionospheric backscatter during geomagnetically quiet periods. Ann. Geophys. 30, 221–233. https://doi.org/10.5194/angeo-30-221-2012.

Koustov, A.V., Ponomarenko, P.V., Ghezelbash, M., Themens, D.R., Jayachandran, P.T., 2014. Electron density and electric field over Resolute Bay and F region ionospheric echo detection with the Rankin Inlet and Inuvik SuperDARN radars. Radio Sci. 49, 1194–1205. https://doi.org/10.1002/2014RS005579.

Koustov, A.V., Ponomarenko, P.V., Graf, C.J., Gillies, R.G., Themens, D.R., 2018. Optimal F region electron density for the PolarDARN radar echo detection near the Resolute Bay zenith. Radio Sci. 53, 1002–1013. https://doi.org/10.1029/2018RS006566.

Koustov, A.V., Sofko, G.J., Andr´e, D., Danskin, D.W., Benkevitch, L.V., 2004. Seasonal variation of HF radar F region echo occurrence in the midnight sector. J. Geophys. Res. Space Phys. 109, A06305. https://doi.org/10.1029/2003JA010337.

Koustov, A.V., Ullrich, S., Ponomarenko, P.V., Nishitani, N., Marcucci, M.F., Bristow, W.A., 2019. Occurrence of F region echoes for the polar cap SuperDARN radars. Earth Planets Space 71, 112. https://doi.org/10.1186/s40623-019-1092-9.

Lamarche, L.J., Makarevich, R.A., 2015. Solar control of F region radar backscatter: further insights from observations in the southern polar cap. J. Geophys. Res. Space Phys. 120, 9875–9890. https://doi.org/10.1002/2015JA021663.

de Larquier, S., Ponomarenko, P., Ribeiro, A.J., et al., 2013. On the spatial distribution of decameter-scale subauroral ionospheric irregularities observed by SuperDARN radars. J. Geophys. Res. 118, 5244–5254. https://doi.org/10.1002/jgra.50475.

Lockwood, M.B., Lanchester, S., Morley, S.K., Milan, S.E., Lester, M., Frey, H.U., 2006. Modeling the observed proton aurora and ionospheric convection responses to changes in the IMF clock angle: 2. Persistence of ionospheric convection K.T. J. Geophys. Res. 111, A02306. https://doi.org/10.1029/2003JA010307.

Liu, L., He, M., Yue, X., Ning, B., Wan, W., 2010. Ionosphere around equinoxes during low solar activity. J. Geophys. Res. 115, A09307. https://doi.org/10.1029/2010JA015318.

Luan, X., Wang, W., Burns, A., Solomon, S., Zhang, Y., Paxton, L.J., 2010. Seasonal and hemispheric variations of the total auroral precipitation energy flux from TIMED/GUVI. J. Geophys. Res. Space Phys. 115, A11304. https://doi.org/10.1029/2009JA015063.

Milan, S.E., Yeoman, T.K., Lester, M., Thomas, E.C., Jones, T.B., 1997. Initial backscatter occurrence statistics for the CUTLASS HF radars. Ann. Geophys. 15, 703–718. https://doi.org/10.1007/s00585-997-0703-0.

Nava, B., Cösson, P., Radicella, S., 2008. A new version of the NeQuick ionosphere electron density model. J. Atmos. Sol. Terr. Phys. 70, 1856–1862. https://doi.org/10.1016/j.jastp.2008.01.015.

Nishitani, N., Ruohoniemi, J.M., Lester, M., Baker, J.B.H., Koustov, A.V., Shepherd, S.G., Chisham, G., Hori, T., Thomas, E.G., Makarevich, R.A., Marchaudon, A., Ponomarenko, P., Wild, J., Milan, S., Bristow, W.A., Devlin, J., Miller, E., Greenwald, R.A., Ogawa, T., Kikuchi, T., 2019. Review of the accomplishments of mid-latitude super dual auroral radar network (SuperDARN) HF radars. Progr. Earth Planet Sci. 6, 27. https://doi.org/10.1186/s40645-019-0270-5.

Ossakow, S.L., Chaturvedi, P.K., 1979. Current convective instability in the diffuse aurora. Geophys. Res. Lett. 6, 332–334. https://doi.org/10.1029/GL006i004p00332.

Ponomarenko, P.V., St Maurice, J.P., Hussey, G.C., Koustov, A.V., 2010. HF ground scatter from the polar cap: ionospheric propagation and ground surface effects. J. Geophys. Res. Space Phys. 115, A10310. https://doi.org/10.1029/2010JA015828.

Ponomarenko, P.V., St-Maurice, J.P., Waters, C.L., et al., 2009. Refractive index effects on the scatter volume location and Doppler velocity estimates of ionospheric HF backscatter echoes. Ann. Geophys. 27, 4207–4219. https://doi.org/10.5194/angeo-27-4207-2009.

Prikryl, P., Jayachandran, P.T., Mushini, S.C., Pokhotelov, D., MacDougall, J.W., Donovan, E., Spanswick, E., St-Maurice, J.P., 2010. GPS TEC, scintillation and cycle slips observed at high latitudes during solar minimum. Ann. Geophys. 28, 1307–1316. https://doi.org/10.5194/angeo-28-1307-2010.

Ruohoniemi, J.M., Greenwald, R.A., 1997. Rates of scattering occurrence in routine HF radar observations during solar cycle maximum. Radio Sci. 32, 1051–1070. https://doi.org/10.1029/97RS00116.

Rush, C., Fox, M., Bilitza, D., et al., 2008. Ionospheric mapping – an update of foF2 coefficients. Telecommun. J. 56, 179–182.

Shepherd, S.G., 2014. Altitude-adjusted corrected geomagnetic coordinates: definition and functional approximations. J. Geophys. Res. Space Phys. 119, 7501–7521. https://doi.org/10.1002/2014JA020264.

Shim, J.S., Kuznetsova, Rastätter, L., et al., 2011. CEDAR Electrodynamics Thermosphere Ionosphere (ETI) Challenge for systematic assessment of ionosphere/thermosphere models: NmF2, hmF2, and vertical drift using ground-based observations. Space Weather 9, S12003. https://doi.org/10.1029/2011SW000727.

Shim, J.S., Kuznetsova, Rastätter, L., et al., 2012. CEDAR Electrodynamics Thermosphere Ionosphere (ETI) Challenge for systematic assessment of ionosphere/thermosphere models: electron density, neutral density, NmF2, and hmF2 using space based observations. Space Weather 10, S10004. https://doi.org/10.1029/2012SW000851.

Shubin, V.N., Karpachev, A.T., Tsybuly, K.G., 2015. Global model of the F2 layer peak height for low solar activity based on GPS radio-occultation data. J. Atmos. Sol. Terr. Phys. 104, 106–111. https://doi.org/10.1016/j.jastp.2013.08.024.

SuperDARN Data Analysis Working Group Participating members E.G. Thomas P.V. Ponomarenko D.D. Billett E.C. Bland A.G. Burrell K. Kotyk et al. SuperDARN radar software Toolkit (RST) 4.2 August 24, (Version v4.2). Zenodo http://doi.org/10.5281/zenodo.1403226 2018

Themens, D.R., Jayachandran, P.T., Nicolls, M.J., MacDougall, J.W., 2014. A top to bottom evaluation of IRI 2007 within the polar cap. J. Geophys. Res. Space Phys. 119, 6689–6703. https://doi.org/10.1002/2014JA020052.

Tsagouri, I., Goncharenko, L., Shim, J.S., Belehaki, A., Buresova, D., Kuznetsova, M.M., 2018. Assessment of current capabilities in modeling the ionospheric climatology for space weather applications: foF2 and hmF2. Space Weather 16, 1930–1945. https://doi.org/10.1029/2018SW002035.

Tsunoda, R.T., 1988. High latitude irregularities: a review and synthesis. Rev. Geophys. 26, 719–760. https://doi.org/10.1029/RG026i004p00719.